

Journal of Neurophysiology

JN-01065-2004.R1

Originally submitted on October 10, 2004

Revised version submitted on February 14, 2005

Accepted on February 27, 2005

### **Effects of inhibitory feedback in a network model of avian brainstem**

Vasant K. Dasika<sup>1,2</sup>, John A. White<sup>1,3</sup>, Laurel H. Carney<sup>4</sup>, and H. Steven Colburn<sup>1,2</sup>

<sup>1</sup>Department of Biomedical Engineering, <sup>2</sup>Hearing Research Center, <sup>3</sup>Center for BioDynamics, Boston University, 44 Cummington Street Boston, MA, 02215; <sup>4</sup>Depts. of Biomedical & Chemical Engineering and Electrical Engineering & Computer Science, Institute for Sensory Research, Syracuse University, 621 Skytop Road Syracuse, NY

13244-5290

Running head: Inhibitory feedback in a network model

Correspondence to: VKD

Telephone: 617-353-5918

Facsimile: 617-353-6766

E-mail: vdasika1974@yahoo.com

## Abstract

The avian auditory brainstem consists of a network of specialized nuclei, including nucleus laminaris (NL) and superior olivary nucleus (SON). NL cells show sensitivity to interaural-time-difference (ITD), a critical cue that underlies spatial hearing. SON cells provide inhibitory feedback to the rest of the network. Empirical data suggest that feedback inhibition from SON could increase the ITD sensitivity of NL across sound-level. Using a bilateral network model, we assess the effects of SON feedback inhibition. Individual cells are specified as modified leaky-integrate-and-fire neurons whose time constants and thresholds vary with inhibitory input. Acoustic sound-level is reflected in the discharge rates of the model auditory-nerve fibers which innervate the network. Simulations show that with SON inhibitory feedback, ITD sensitivity is maintained in model NL cells over a threefold range in auditory-nerve discharge rate. In contrast, without SON feedback inhibition, ITD sensitivity is significantly reduced as input rates are increased. Feedback inhibition is most beneficial in maintaining ITD sensitivity at high input rates (simulating high sound-levels). With SON inhibition, ITD sensitivity is maintained for both interaurally balanced inputs (simulating an on-center sound source) and interaurally imbalanced inputs (simulating a lateralized source). Further, the empirically observed temporal buildup of SON inhibition and the presence of reciprocal inhibitory connections between the ipsilateral and contralateral SON both improve ITD sensitivity. In sum, our network model shows that inhibitory feedback can substantially increase the sensitivity and dynamic range of ITD coding in the avian auditory brainstem.

# 1 Introduction

The submillisecond difference in the time of arrival of sound to the two ears, interaural-time-difference (ITD), is a critical cue in the localization and processing of sound sources (cf. Blauert 1997). Nucleus laminaris (NL), the avian homolog of the mammalian medial superior olive (MSO), is the first neural center to receive input from the two ears. Fibers from nucleus magnocellularis (NM) project bilaterally and provide phase-locked, glutamatergic, excitatory input to NL. Single neurons in NL show sensitivity to ITD by performing coincidence detection (Jeffress 1948) on the input from left and right NM (Sullivan and Konishi 1984; Carr and Konishi 1990). Empirical data indicate that ITD sensitivity is maintained in NL over a 50 dB range in sound-level (Peña et al. 1996). However, simple coincidence models (Reed and Durbeck 1995; Peña et al. 1996) lose ITD sensitivity as the discharge rate of NM fibers monotonically increases three-fold or more with sound-level (Warchol and Dallos 1990).

Two mechanisms have been demonstrated to maintain ITD sensitivity in models of NL despite variations in sound-level. First, synaptic depression has been observed in the NM to NL synapse (Kuba et al. 2002; Cook et al. 2003). When synaptic depression was included in a model of NL, response to ITD was consistent over a three-fold range of input discharge rate (Cook et al. 2003). Without depression, however, ITD sensitivity degraded with elevated input rate. A second mechanism which preserved ITD sensitivity in model NL across sound-level was the inclusion of inhibitory input. ITD sensitivity was maintained in a model of NL when a sound-level-dependent, feed-forward inhibitory input from the superior olivary nucleus (SON) was included (Peña et al. 1996). In contrast, ITD

sensitivity was lost as sound-level was increased without the inclusion of SON inhibition. Inhibition was also used in a model of mammalian MSO (Zhou and Colburn 2003; Colburn et al. 2004) to predict ITD-dependent, non-monotonic, rate-level curves observed empirically (Goldberg and Brown 1969). While Grau-Serrat and colleagues (2003) included feedback inhibition to their biophysically detailed model of NL, the influence of sound-level dependence was not explicitly explored.

Although modeling studies have demonstrated the effects of synaptic depression (Cook et al. 2003) and feed-forward inhibition on ITD sensitivity across sound-level (Peña et al. 1996; Zhou and Colburn 2003; Colburn et al. 2004), this study is the first to examine ITD sensitivity and sound-level dependence in the context of network feedback inhibition observed in the avian brainstem. Anatomy and physiology from the chicken (Yang et al. 1999; Monsivais et al. 2000) indicate a negative-feedback, gain-control role for the SON, which appears to be well suited to maintain ITD sensitivity in NL despite changes in sound-level. The SON receives excitation from NL and nucleus angularis (NA) and provides feedback inhibition to NL, NM, and NA (Lachica et al. 1994; Yang et al. 1999; Monsivais et al. 2000; Burger et al. 2005). The SON also projects to contralateral SON, which may serve to decrease the effects of level imbalances<sup>1</sup> to the two sides (Lachica et al. 1994; Monsivais et al. 2000; Burger et al. 2005). In contrast, the mammalian system is widely believed to have primarily ascending excitation and inhibition to MSO (cf. Grothe 2003).

Physiological data suggest that the SON is suited to perform gain-control. Single neurons in SON appear able to reflect the average discharge rate of their inputs, as they have relatively long time-constants (on the order of 30 ms) and EPSP durations (Yang et al. 1999). SON inhibition is GABAergic, which has been demonstrated to: 1) decrease the

time constant in NL and NM neurons (Yang et al. 1999; Monsivais et al. 2000), and 2) increase the threshold in NM neurons (Monsivais and Rubel 2001). GABAergic inhibitory responses are relatively slow, lasting on the order of tens to hundreds of milliseconds (Hyson et al. 1995; Funabiki et al. 1998; Yang et al. 1999; Monsivais et al. 2000; Lu and Trussell 2001; Monsivais and Rubel 2001), in contrast to the rapid (approximately 1 ms long) glutamatergic responses seen in NL, NM, and NA (Raman et al. 1994). In fact the SON-originated, slow GABAergic input has been demonstrated to modulate NL neurons by reducing the amplitude and shortening the temporal duration of the EPSP induced by glutamatergic input (Yang et al. 1999). As we show, the slow modulation of the fast glutamatergic response by GABAergic input from SON is consistent with the presumed role of the SON in maintaining temporal sensitivity in NL and NM, particularly over variations in sound-level. SON activity, moreover, modulates the GABAergic inhibitory response. A stronger SON input or a higher rate of SON inputs has been shown to prolong and strengthen the observed inhibitory response (Yang et al. 1999; Lu and Trussell 2000; Monsivais et al. 2000).

Through computational modeling, we investigate the influence of inhibitory feedback from the SON to the rest of the avian auditory brainstem network. Both balanced and imbalanced level conditions are tested since ITD sensitivity has been empirically observed in NL under both conditions (Peña et al. 1996; Viete et al. 1997). Our network model shows that feedback inhibition from the SON can significantly expand the dynamic range of the avian ITD coding system.

## 2 Methods

We calculated the response of each neuron in the network to a steady-state pure tone of varying level. The network was comprised of single model neurons that were designed to include the three attributes described in the Introduction: first, the fast glutamatergic-like membrane depolarizing response, critical for phase-locking in NM and for ITD sensitivity in NL; second, the slow GABAergic inhibitory response to SON inputs (seen in NM and NL); and third, the temporal buildup of this inhibitory response with increasing SON stimulation. A block diagram of the network model connectivity is shown in Fig. 1. The neural connectivity was based on recent knowledge of the ITD pathway of the chicken (Monsivais et al. 2000).

Table 1 provides a summary of the parameter values used for the simulations in this study unless otherwise noted. Parameters were divided into four categories: input parameters, excitatory connection parameters, inhibitory connection parameters, and cell parameters.

### 2.1 Input model

Auditory-nerve (AN) inputs were generally half-second-duration sets of discharge times delivered to model neurons in the network. As in Peña et al. (1996) two categories of inputs were used: non-phase-locked inputs which were delivered to NA and phase-locked-inputs which were delivered to NM. Non-phase-locked inputs were generated by a homogeneous Poisson process with no dead-time. For phase-locked inputs, the response of a single input fiber was constructed by assuming a periodic input with

frequency  $f$ , an average discharge rate  $R$ , and a temporal jitter random variable with a standard deviation  $\sigma$ . On each period, the probability that an event occurred equaled  $R/f$ , ( $f \geq R$ ). If an event occurred, it was placed at a phase determined by the temporal jitter added to the specified average phase. The jitter was specified as a zero-mean, normal random variable with a standard deviation chosen to provide the desired vector strength ( $VS$ ), specifically,  $\sigma = \frac{1}{2\pi f} \sqrt{-2 \ln(VS)}$ . The jitter was statistically independent from period to period. Input refractoriness was modeled by eliminating inputs that were generated within 1 ms of the previous event on that particular fiber. As given in Table 1A,  $f = 600$  Hz and  $VS = .76$  for most of our phase-locked input cases, as in Cook and colleagues (2003). When multiple-fiber inputs were considered, multiple, statistically identical and independent fibers were used.

The discharge rates of phase-locked and non-phase-locked categories of inputs were used to reflect the sound-level of the simulated acoustic stimulus. Rate varied over a three-fold range (150 to 450 spikes/sec), as in the Cook et al. (2003) model. On a given side (i.e., the left or the right), the rates for both phase-locked and non-phase-locked inputs were equal. Input rate conditions to the two sides were usually denoted as a pair of rates. For example, “150, 450 spikes/sec” means that the rate was 150 spikes/sec for the left AN inputs, and 450 spikes/sec for the right AN inputs.

Pre-generated sets of input times were used for a given stimulus. This made it possible to test the result of different network configurations to the *same* sets of inputs. Consequently, the effects due to changes in the network configuration could be isolated without the additional variability that would occur if different samples of input-time-sets were used. Simulations tested responses to driven-activity only — spontaneous activity

conditions were not tested. Furthermore, only binaural stimulation cases are presented.

## 2.2 Network model

The network model is shown in Fig. 1 with model cells representing NL, NM, NA, and SON on each side. The network was symmetric, with cells and connections on the left side mirroring those on the right side. Three independent, phase-locked auditory-nerve fibers excited each NM cell. Ten separate NM cells were modeled per side, and all ten NM cells per side bilaterally excited a single NL cell on each side. Different propagation delays could be specified from the NM cells on one side to the left and right NL cells. Each NL cell had a best ITD that was equal in magnitude but opposite in sign to its mirroring NL cell on the other side. The NL cell on each side excited the SON cell on the same side. A single, non-phase-locked, auditory-nerve input fiber from each side excited a single NA cell, and each NA cell excited the SON cell on the same side. Each SON cell inhibited ipsilateral NL, NM, NA, and contralateral SON. Simulations also tested the effects of no SON-feedback inhibition. Where noted in the Results, limited additional simulations tested the effects of other SON-feedback configurations.

The following four subsections describe: 1) the structure of a single model cell, 2) the simulation protocol, 3) an overview of the model parameters used, and 4) the data analysis used.

### 2.2.1 Structure of model cell

Each model cell in the network was an “adapting leaky-integrate-and-fire (LIF)” cell. An adapting LIF cell was defined as a standard LIF cell (cf. Tuckwell 1988) whose

parameters were affected by SON input and thereby varied with time.

Consider first a standard LIF cell, which is described by a single state variable, membrane voltage  $V_m(t)$ . An excitatory input event causes an instantaneous increment  $V_m^{inc}$  in membrane voltage. Between inputs, membrane voltage decays toward zero with a fixed membrane time constant  $\tau_m$ . The differential equation describing the membrane voltage of a standard LIF cell is given by Eq. 1:

$$\frac{dV_m(t)}{dt} = \frac{-V_m(t)}{\tau_m} + V_m^{inc} \sum_{\text{all } k} \delta(t - t_k), \quad (1)$$

where  $\delta(\cdot)$  represents the Dirac delta or impulse function (cf. Dayan and Abbott 2001) and  $t_k$  is the time of the  $k$ -th input. The resulting function  $V_m(t)$  has the characteristic shape of step increments of height  $V_m^{inc}$  at the times of input events with an otherwise continuous exponential decay (with time constant  $\tau_m$ ) to rest (which is normalized to zero in Eq. 1). If the membrane voltage crosses a specified threshold  $V_T$ , then an output event is generated and the membrane voltage is set to zero and held there for the duration of the absolute refractory period. Panel E of Fig. 2 illustrates the response properties of a standard LIF model to the input pattern shown at the bottom of the panel, namely: the characteristic shape of  $V_m(t)$  (thick black line), the constant threshold  $V_T$  (thin black line, equal to 1 here), the membrane voltage reset values (equal to 0), and the refractory period (equal to 1 ms here) following a cell discharge (discharges are indicated at the top of the panel by the ‘x’ symbols).

The *adapting* LIF model used in the present study extended the standard LIF model such that inhibitory input from the SON elicited changes in the time constant  $\tau_m$  and the threshold  $V_T$ . Based on empirical observations described in the Introduction, we

assumed that SON inhibitory input decreased the membrane time constant  $\tau_m$  and increased the threshold  $V_T$ . Note that both of these changes would reduce the spike rates of the affected neurons. In addition, as greater SON input has been shown empirically to cause longer lasting changes in NL and NM cell response, we assumed that SON input also increased the recovery times of these two parameters ( $\tau_m$  and  $V_T$ ), prolonging the inhibitory response. Otherwise the adapting LIF model operated analogously to the standard LIF model. Excitatory inputs only affected the membrane voltage and did not affect the time constant or the threshold.

Except for a few test cases which are noted in the Results, we generally assumed that SON inputs did not directly affect the membrane voltage. The predominant effect of SON input has been empirically demonstrated to be inhibitory (cf. Introduction), although depolarizing (Hyson et al. 1995; Lu and Trussell 2001; Monsivais and Rubel 2001). GABAergic input from SON opens chloride channels and thereby both decreases the membrane resistance and depolarizes the cell due to chloride efflux (Monsivais et al. 2000; Lu and Trussell 2001; Monsivais and Rubel 2001). Membrane depolarization opens low voltage activated potassium channels, further decreasing the membrane resistance (Monsivais et al. 2000). Depolarization also inactivates voltage-dependent inward (e.g., sodium) currents, increasing the voltage threshold for spiking (Monsivais and Rubel 2001). Since ion channels were not explicitly described in the adapting LIF model, the empirically observed effects of: GABA-induced opening of chloride channels, the resulting membrane depolarization, opening of low voltage activated potassium channels, and inactivation of inward currents, were specified entirely by the net effects of decreasing the membrane time constant and increasing the voltage threshold, *without* directly changing the membrane

voltage. The effects of inhibition in model adapting LIF cells were specified this way because membrane depolarization always moves the cell *closer* to threshold, which would be inconsistent with the empirical observations showing that GABAergic input can move NM cells *away* from threshold.

**State Variables** The adapting LIF model was described by five state variables: 1) the membrane voltage  $V_m$ , 2) the membrane time constant  $\tau_m$ , 3) the time constant  $\tau_{\tau_m}$  that controlled the dynamics of the membrane time constant, 4) the threshold voltage  $V_T$ , and 5) the time constant  $\tau_{V_T}$  that controlled the dynamics of the threshold voltage. In general, when SON inputs were received,  $\tau_m$  decreased so that  $V_m$  decayed more quickly.

Additionally,  $V_T$  increased, making  $V_m$  even less likely to cross threshold. SON input also caused  $\tau_{\tau_m}$  and  $\tau_{V_T}$  to increase so that  $\tau_m$  and  $V_T$  recovered more slowly. The three effects, decreasing  $\tau_m$ , increasing  $V_T$ , and slowing the recovery of  $\tau_m$  and  $V_T$ , modeled the influence of SON inhibition on a target cell, which ultimately decreased cell excitability and firing rate. The state variables of the adapting LIF model are summarized in Table 1B.

Figure 2 illustrates the response of an *isolated* adapting LIF cell model to excitatory (600 Hz, phase-locked) and inhibitory (75 spikes/sec, non-phase-locked) inputs. The left-column panels of Fig. 2A-D show the response of a standard LIF cell (without inhibition). The first (leftmost) panel in row C shows that the membrane voltage  $V_m$  consistently exceeded the threshold  $V_T$  on each stimulus cycle in response to the excitatory 600 Hz inputs, causing a relatively constant response rate of approximately 600 spikes/sec (row D, first panel). However, when inhibition either reduced  $\tau_m$  (second column), increased  $V_T$  (third column), or both (fourth column), significant decreases in the

likelihood of the membrane voltage crossing threshold occurred (see row C, second through fourth panels). The consequent decrease in the response rate can be seen in the rate-versus-time plots in row D. The specification of the model state variables is described in the following paragraphs.

We describe in detail the behaviors of  $\tau_{\tau_m}$  and  $\tau_m$  only. According to our assumptions, the effects of inhibition on the threshold  $V_T$  were similar to the effects on the membrane time constant  $\tau_m$  so that the discussion about  $\tau_m$  is easily translated to  $V_T$ . The recovery time constant  $\tau_{\tau_m}$  of the membrane time constant  $\tau_m$  is shown in row A and was described by two parameters: a (positive) increment amount  $\tau_{\tau_m}^{inc} = 50$  ms, and a ceiling value  $\tau_{\tau_m}^{ceil} = 1$  sec. The membrane time constant  $\tau_m$  shown in row B depended upon the state variable  $\tau_{\tau_m}$ , together with three parameters: an initial value  $\tau_m^0$ , a decrement amount  $\tau_m^{dec}$ , and a floor value  $\tau_m^{floor}$ .

The effect of inhibitory inputs on  $\tau_m$  are illustrated in the second column of Fig. 2. The second panel in row A shows that  $\tau_{\tau_m}$  was instantaneously incremented by the amount  $\tau_{\tau_m}^{inc}$  (50 ms) at the times of inhibitory inputs (the inset shows the first 50 ms of the trace). Whenever  $\tau_{\tau_m}$  was incremented by inhibitory input, the membrane time constant  $\tau_m$  (row B, second panel) was *decremented* by the amount  $\tau_m^{dec}$  (equal to .05 ms here) from its initial value of  $\tau_m^0$  (equal to 1 ms here). Ceiling and floor values were imposed to limit state variable excursions: if  $\tau_{\tau_m}$  ever was incremented beyond  $\tau_{\tau_m}^{ceil}$  (1 sec), it was set equal to  $\tau_{\tau_m}^{ceil}$ ; likewise, if  $\tau_m$  ever was decremented to be less than  $\tau_m^{floor}$  (equal to .3 ms here), it was set equal to  $\tau_m^{floor}$ .

Between inhibitory inputs, both  $\tau_{\tau_m}$  and  $\tau_m$  decayed exponentially toward their initial values (zero and  $\tau_m^0$  respectively), both with a time constant *equal* to the value of  $\tau_{\tau_m}$

immediately after the most recent inhibitory event. As shown in the insets of the second panels of rows A and B, after the first inhibitory input event, both  $\tau_{\tau_m}$  and  $\tau_m$  recovered exponentially with a time constant equal to 50 ms. After the second inhibitory input, these state variables recovered with a *larger* time constant (which was equal to 92 ms in this example based on the updated value of  $\tau_{\tau_m}$ ). The specified form of  $\tau_{\tau_m}$  caused the initial slope of decay of  $\tau_m$  and  $\tau_{\tau_m}$  to be *independent* of the magnitude of the state variables. This is illustrated by the pair of dotted lines shown in the insets of the second panels of rows A and B, where each line depicts the initial slope of decay immediately following inhibitory input. Within a given panel, both dotted lines followed the *same* initial slope of decay, making the lines parallel. This specified increase of the recovery time constant  $\tau_{\tau_m}$  due to inhibitory input provided a simple quantitative description for the empirically observed temporal buildup of inhibitory response (Yang et al. 1999). In contrast, as illustrated by the pair of dotted lines in panel E, a *fixed* time constant exponential response has an initial slope of decay that is *proportional* to the magnitude of the state, causing a fixed decay-time that is independent of state magnitude. A fixed-time-constant model does not exhibit temporal buildup.

**Inhibitory modulators** In our model, stronger inhibition could be modeled as a larger  $\tau_m^{dec}$  parameter which would cause a larger decrement in  $\tau_m$  due to an SON inhibitory input. With ongoing inhibitory input, a smaller  $\tau_m^{floor}$  value could allow  $\tau_m$  to decrease further. Dynamics also affect the strength of inhibition. An SON input increases  $\tau_{\tau_m}$  by the amount  $\tau_{\tau_m}^{inc}$ . A larger value of  $\tau_{\tau_m}^{inc}$  increases the duration of the inhibitory response since  $\tau_m$  decays exponentially with a time constant equal to the latest incremented value of

$\tau_{\tau_m}$ . Ongoing SON input causes summation in  $\tau_m$  and  $\tau_{\tau_m}$ , increasing both the magnitude and duration of the inhibitory response. Moreover, the amount of summation is largest when  $\tau_{\tau_m}^{ceil}$  is large relative to the (instantaneous) value of  $\tau_{\tau_m}$ , furthering the temporal buildup. The ceiling value of  $\tau_{\tau_m}$  can consequently affect the duration and magnitude of the inhibitory response (see Results).

A substantial, steady rate of inhibitory input as used in Fig. 2 could cause a significant change in both  $\tau_m$  and  $\tau_{\tau_m}$  over time. As illustrated in the second and fourth panels of Fig. 2B,  $\tau_m$  was decreased toward and maintained at its floor value (0.3 ms) as  $\tau_{\tau_m}$  (Fig. 2A) was increased toward and maintained at its ceiling value, slowing the recovery of both states. Because the value of the membrane voltage  $V_m$  was dependent on  $\tau_m$ , the likelihood of  $V_m$  to exceed threshold decreased as  $\tau_m$  decreased (compare the first and second panels in row C; also, compare the third and fourth panels of row C). Note that similar effects of inhibition can be seen on the threshold,  $V_T$ , by comparing the first and third, and the second and fourth panels in row C.

**Derivation of  $V_m$**  Equation 2 describes the membrane voltage  $V_m$  of the adapting LIF model whose membrane time constant  $\tau_m$  varied with time:

$$\frac{dV_m(t)}{dt} = \frac{-V_m(t)}{\tau_m(t)} + V_m^{inc} \sum_{\text{all } k} \delta(t - t_{exc,k}), \quad (2)$$

where  $t_{exc,k}$  is the time of the  $k$ -th excitatory input. (Since excitatory and inhibitory inputs were defined to have different actions in the adapting LIF model, we separately denote their ordered sets of times as  $\{t_{exc}\}$  and  $\{t_{inh}\}$  respectively.) As described above,  $\tau_m(t)$  was a piecewise exponential function. A piecewise exponential form for  $\tau_m(t)$  was purposefully specified because it enabled us to derive an analytical solution<sup>2</sup> for  $V_m$  in Eq. 2

in terms of  $V_m$  at the previous input event. The membrane voltage  $V_m$  at some time  $t$  after the time of the last input event (whether excitatory or inhibitory at time  $t_k$ ), and before the time of the next input event ( $t_{k+1}$ ), was solved for (see Appendix for details), yielding:

$$\begin{aligned} V_m(t) &= g(t)V_m(t_k^+) \exp\left(-(t - t_k)/\tau_m^0\right) \quad \text{for } t_k^+ \leq t < t_{k+1}, \text{ where} \\ g(t) &= \left[ \frac{\tau_m(t_k^+)}{\tau_m(t)} \right]^{\tau_{\tau_m}(t_{inh,rec}^+)/\tau_m^0}, \end{aligned} \quad (3)$$

where  $\tau_{\tau_m}(t_{inh,rec}^+)$  was the value of  $\tau_{\tau_m}$  immediately after the most recent inhibitory event.

Equation 3 is written in a form where the voltage arising from a standard LIF decay,

$V_m(t_k^+) \exp(-(t - t_k)/\tau_m^0)$ , is multiplied by a factor  $g(t)$  that was always less than or equal

to one. The factor  $g(t)$  was less than or equal to one because  $\tau_m$  increased toward  $\tau_m^0$

between inhibitory inputs (as shown in detail in the inset of the second panel, row B).

Inhibitory input created a ‘‘leakier’’ cell membrane, which caused the membrane voltage to

decay faster than it otherwise would without inhibitory input. As a result, the membrane

voltage was generally lower and crossed threshold less often when the time constant varied

(row C, second panel), compared to when the time constant was fixed (row C, first panel),

causing a decreased firing rate (row D, second panel versus the first panel). Differences

were also apparent in the detailed voltage responses resulting from a decreased (Fig. 2F,

thick black line) versus unaffected (Fig. 2F, thick gray line) membrane time constant.

### 2.2.2 Simulation protocol

Computation of the network response was based on an array of ordered event times.

The array initially contained the input times delivered to the network. The array was

updated and reordered every time an event was generated within the network. Specifically,

after adding appropriate synaptic/propagation delays to the input times, the arrival times at the target cells were ordered in the array. Each array element held the event time, along with the input-cell and target-cell information associated with that event. The first event was processed, causing all five state variables at the target cell to be updated in ways depending on the specific target-cell/input-cell combination. The target cell was then checked for the occurrence of an output event (an output event occurred if  $V_m$  equaled or exceeded  $V_T$ ). If an output event occurred, appropriate synaptic/propagation delay(s) for the current target-cell's target(s) were added, and these time(s) were inserted sequentially in the array. Refractoriness was included in a manner similar to that in a standard LIF model: excitatory inputs arriving at a given cell (which normally incremented the membrane voltage) were ignored for a specified deadtime after the last output at that same cell. During the refractory period, however, inhibitory inputs were processed as usual (i.e.,  $\tau_{\tau_m}$ ,  $\tau_m$ ,  $\tau_{V_T}$ , and  $V_T$  were decaying and were incremented whenever inhibitory inputs occurred). The next occurring temporal event in the array was then processed. This update cycle was continued until a specified simulation duration was reached.

### 2.2.3 Parameters

The increment and ceiling values for the time constants  $\tau_{\tau_m}$  and  $\tau_{V_T}$  were generally specified as 50 ms and 1 sec, respectively, based on empirical data of NL responses when SON was stimulated (Yang et al. 1999). Additional simulations (noted in the Results) tested values other than 1 sec for the ceiling values of the recovery time constants (e.g., ceiling values of 50 ms were specified to fix the recovery time constants at 50 ms).

SON cell parameters were based on *in vitro* data (Yang et al. 1999). NL parameters

were based on *in vitro* data (Reyes et al. 1996; Yang et al. 1999). NM cell parameters were based on *in vivo* (Joris et al. 1994) and *in vitro* (Reyes et al. 1994) data. Finally our specification of NA parameters was consistent with *in vitro* data (Soares et al. 2002), and elicited a discharge rate range that was compatible with that observed *in vivo* (Warchol and Dallos 1990).

In most of our network simulations, the right NL was modeled as having a best delay of  $+100 \mu\text{s}$ , i.e., inputs arrived coincidentally at the right NL when the right side inputs were delayed by  $100 \mu\text{s}$  compared to the left side inputs. The left NL was modeled with a  $-100 \mu\text{s}$  best delay, i.e., inputs arrived coincidentally at the left NL when the left side inputs were delayed by  $100 \mu\text{s}$  with respect to the right side inputs. Left and right NL best delays were based on empirical data (Overholt et al. 1992; Hyson et al. 1994). As noted in the Results, additional simulations also tested the case when the NL cells on both the left and right sides were tuned to a best ITD of 0, and thus had the *same* best-ITD tuning.

#### 2.2.4 Data Analysis

Simulations showed that cell responses progressively changed over the course of hundreds of milliseconds with the inclusion of SON feedback inhibition. To capture this slow variation, cell response rates were plotted using 100 ms long moving-averaged windows that were half-overlapped. Errorbars indicate plus and minus one standard error about the mean rate over the specified number of repetitions (each repetition used an independent stimulus sample). (Figures 3 and 4 were generated using 10 repetitions. Figure 5 was generated using 98 repetitions [error bars are not shown for clarity]. Figures 6 to 8 were generated using 45 repetitions.)

### 3 Results

Simulations consisted of applying bilateral auditory nerve (AN) input to the left and right sides, while monitoring network cell responses. Input rate generally reflected the intensity of the auditory stimulus. Rates were either the same to the two sides (balanced inputs), or different to the two sides (imbalanced inputs). Simulations tested the network cells' responses both with and without the inclusion of SON inhibitory feedback. For a given input rate condition, two different stimulus ITDs were generally presented so that inputs from the left and right sides arrived either in-phase (i.e., coincidently) at the right NL, or out-of-phase (i.e., with a  $180^\circ$  phase shift) at the right NL.

We present three main results. First, SON feedback inhibition maintained rate-ITD modulation in NL over a three-fold range in AN input rates, whereas without SON feedback, modulation was lost at high AN rates. Second, with the inclusion of SON inhibition, rate-ITD modulation in NL improved progressively over time due to the temporal buildup of the inhibitory response. Finally, the presence of reciprocal inhibitory connections between SONs improved the robustness of rate-ITD modulation in NL on both sides of the brainstem.

#### 3.1 SON inhibition and rate-ITD modulation

Figures 3 and 4 show summary responses of all cell types in the network for low-rate (150 spikes/sec to each NM and NA cell) and high-rate (450 spikes/sec to each NM and NA cell) balanced inputs, respectively. We defined the presence of rate-ITD modulation in NL as a consistently *higher* response to in-phase stimuli compared to out-of-phase stimuli

over time. For low-rate inputs (Fig. 3), there was generally little difference in cell responses caused by SON-feedback as indicated by the similarity of the associated solid and dashed traces. Significant rate-ITD modulation was observed in *both* the right NL (which has a best-delay equal to the in-phase stimulation delay) and the left NL (which has a best-delay that is  $200 \mu\text{s}$  away from the in-phase stimulation delay) in response to low-rate inputs, both with and without the inclusion of SON-feedback. In-phase responses (lines with no symbols) were consistently greater than out-of-phase responses (lines with triangles). In contrast, with high-rate inputs of 450 spikes/sec to each side (Fig. 4), rate-ITD modulation in the NL on both sides was lost without SON inhibitory feedback. In- and out-of-phase rates were both generally saturated at 600 spikes/sec (solid lines). With the inclusion of SON inhibitory feedback, however, rate-ITD modulation in NL on both sides was regained (Fig. 4, dashed lines). Inclusion of SON feedback generally reduced rates in all cells in the network with time (cf. Fig. 4). The resulting decrease in NM rate, together with SON directly inhibiting NL, maintained rate-ITD modulation in NL at high levels.

Figure 5 shows rate-ITD curves in the right NL for different epochs of time during the response with SON feedback. Specifically, the response rate at ITDs intermediate to the in-phase and out-of-phase delays was computed at each of the moving average windows. Responses decreased smoothly from the in-phase delay to the out-of-phase delay at a given time-point, consistent with rate-ITD curves typically observed in NL. Rate-ITD curves were symmetric for balanced inputs, both with and without inhibitory feedback (cf. Fig. 5). Small asymmetries in rate-ITD curves were initially observed to imbalanced inputs. As the influence of inhibitory feedback increased over time, NM rates on the two sides became more equal, decreasing any asymmetry initially observed in rate-ITD curves

from imbalanced inputs [150, 450 spikes/sec inputs were tested, data not shown].

The next set of simulations explored multiple stimulus levels. We introduced a percentage-of-modulation metric<sup>3</sup> to reflect the *relative* amount of rate-ITD modulation, which is not conveyed by absolute rate information alone. At a given timepoint, for each stimulus presentation, percentage-of-modulation is defined as the rate resulting from in-phase stimulation minus the rate resulting from out-of-phase stimulation divided by the in-phase rate and multiplied by 100. This measure better reflects the modulation. For example, the same absolute rate difference of 20 spikes/sec occurs from an in-phase rate of 30 spikes/sec and out-of-phase rate of 10 spikes/sec, as it does for an in-phase rate of 600 spikes/sec and out-of-phase rate of 580 spikes/sec. By contrast, the percentage-of-modulation for these two examples is 67% and 3% respectively, reflecting the larger relative amount of modulation in the former case.

Figure 6 shows the in- and out-of-phase rates for the right NL cell for several balanced and imbalanced input level conditions. Figure 7 shows the percentage-of-modulation amounts for the same conditions as Fig. 6. Without SON feedback (solid lines), the in- and out-of-phase rates converged (Fig. 6) and the amount of rate-ITD modulation generally decreased (Fig. 7) as the average input rate to the two sides was increased (see in order, panels C, D, F, and E in Figs. 6 and 7). For high input rates, modulation was reduced (e.g., Fig. 7D, solid line) or lost entirely (e.g., Fig. 7E, solid line). In contrast, with the inclusion of SON inhibitory feedback (dashed lines), rate-ITD modulation in NL was maintained across input rate conditions. At the highest input rates to both sides, inclusion of SON-feedback caused the most pronounced improvement in NL rate-ITD modulation, from essentially no modulation without SON-feedback, to nearly 30

percent modulation with feedback (Fig. 7E, solid versus dashed line). Rate-ITD modulation generally improved with the inclusion of SON feedback as input rates increased for both balanced (Figs. 7A,C,E) and imbalanced (Figs. 7B,D,F) conditions to the two sides.

Results were also obtained for a network in which the left and right NL were tuned to the *same* best ITD. These results (not shown) also demonstrated improvement in NL rate-ITD modulation to higher level balanced and imbalanced inputs with SON-feedback.

### 3.2 Rate-ITD modulation improves over time

Our simulations indicated that SON feedback inhibition improved rate-ITD modulation in NL progressively over time (Figs. 6 and 7). Significant increases in the amount of rate-ITD modulation often occurred during the first 200 ms (e.g., see Fig. 7D,E,F arrows). More gradual changes followed until steady-state responses were reached (after about one second, based on simulations with longer duration stimuli [data not shown]). Long-lasting decreases in responses occurred because the cells in the network were interconnected and continuously influencing each other, consistent with the the SON inhibitory feedback structure. Responses typically took longer to reach steady state at higher input levels (panels D,E,F in Figs. 6 and 7), compared to lower input levels (panels A,B,C in Figs. 6 and 7). This is because cells needed modulation of their parameters over a wider range for NL to show rate-ITD modulation at high levels compared to at low levels. In contrast, the response from an *isolated* adapting LIF cell model (Fig. 2) driven by relatively high, constant rates of excitatory and inhibitory input reached steady state more rapidly (within  $\approx 0.25$  sec).

A key mechanism underlying the increase in rate-ITD modulation in NL over time in the network was the temporal buildup of SON inhibitory response. If SON inhibition was specified *without* the temporal buildup, such that the membrane time constant and the threshold states for all cells receiving inhibition always decayed with a *fixed* time constant of 50 ms (i.e., by fixing  $\tau_{\tau_m}^{ceil}$  and  $\tau_{V_T}^{ceil}$  equal to 50 ms), then the extent of rate-ITD modulation in NL was significantly reduced. The reduction in modulation was found for both large balanced input rates of 450 spikes/sec to the two sides (shown in Figs. 6E and 7E by dotted lines), and for large imbalanced rates of 150, 450 spikes/sec [data not shown]. Rate-ITD modulation amounts with feedback but no temporal buildup were slightly larger than without-feedback conditions (compare dotted and solid lines in Fig. 7E). Modulation with SON feedback but no temporal buildup, however, was significantly less than when SON feedback was specified *with* temporal buildup (compare dotted and dashed lines in Fig. 7E). Furthermore, when we tested intermediate values of  $\tau_{\tau_m}^{ceil}$  and  $\tau_{V_T}^{ceil}$ , the maximal percentage-of-modulation monotonically increased with the recovery time-constant ceiling, while the time to reach steady state increased (100, 200, and 500 ms were tested, data not shown). The response for the 500 ms ceiling value actually equaled the response for the 1 sec ceiling value indicating that recovery time constants did not typically exceed 500 ms in our network simulations (for both 450, 450 spikes/sec and 150, 450 spikes/sec, not shown). In summary, the temporal buildup of inhibition lasting hundreds of milliseconds, appeared to allow a single SON cell, despite a relatively low maximal firing rate (of approximately 80 spikes/sec), to consistently inhibit the NL, NM, NA, and contralateral SON, which in turn, significantly improved rate-ITD modulation in NL.

### 3.3 Reciprocal inhibitory connections between SONs

We also explored the importance of the reciprocal inhibitory connections between the ipsilateral and contralateral SONs on rate-ITD modulation. These connections were found to improve rate-ITD modulation in the NL on *both* sides of the brainstem. Figure 8 shows rate responses and modulation amounts in both the right and left NL cells for an input rate-imbalanced case for three SON feedback conditions: no feedback, feedback with no reciprocal (SON-to-SON) connections (i.e., ipsilateral only feedback), and full SON-feedback (i.e., including reciprocal connections). With full feedback inhibition, modulation was consistently maintained over time in both the right and the left NL (Fig. 8 all panels, thin dashed lines). With no SON-to-SON reciprocal inhibitory connections, however, rate-ITD modulation was reduced in NL on both sides — especially in the NL on the side not tuned to the stimulus ITD (Fig. 8 left panels, thick dashed lines). This ipsilateral-only inhibitory condition caused a dip in the modulation over time, driven to the extent where the modulation at 0.35 sec was significantly reduced (right NL) and lost entirely (left NL). Without the reciprocal inhibitory SON projections, a reduction in rate-ITD modulation was also found for level-balanced cases of 300, 300 spikes/sec and 450, 450 spikes/sec [data not shown]. A decrease in the regulation of SON feedback arising from the ipsilateral only feedback condition reduced the in-phase response excessively, ultimately reducing modulation.

Because it is not conclusively known whether the SON-to-SON projections are inhibitory (cf. Lachica et al. 1994, Burger et al. 2005), we conducted additional simulations in which the reciprocal connections between SONs were specified to be excitatory.

Rate-ITD modulation was generally poor under these excitatory-coupled SON conditions. For the 150, 450 spikes/sec case, an even greater reduction in rate-ITD modulation was observed in both NL for excitatory-connections between the SONs, compared to the no-connections between the SONs case [data not shown]. Furthermore, with excitatory reciprocal connections, while consistent modulation was maintained in the right NL in response to high-level balanced-inputs of 450, 450 spikes/sec, convergence of in- and out-of-phase rates occurred in the left NL, reducing modulation essentially to zero [data not shown]. Modulation was maintained in the left NL, however, with the presence of *inhibitory* connections between the SONs (dashed lines, top left panel of Fig. 4). Reciprocal inhibitory connections between the two SONs therefore appear beneficial in maintaining rate-ITD modulation in NL, both temporally, over the entire stimulus duration, and spatially, across the two sides of the brain.

## 4 Discussion

The avian auditory brainstem network is composed of the NL, NM, NA, and the SON. The SON, which is excited by NL and NA, exerts feedback inhibition on the NL, NM, and NA, and likely on the contralateral SON as well. We analyzed this network circuit using computational modeling. Several key results were found.

Overall, the influence of SON inhibitory feedback on the avian brainstem circuit expands the dynamic range of the ITD coding system to sound-level. SON inhibitory feedback is most beneficial in maintaining ITD sensitivity<sup>4</sup> in NL at high levels, where ITD sensitivity is otherwise lost when feedback is not included. Sensitivity to ITD is maintained for both balanced and imbalanced levels to the two sides, with the inclusion of SON inhibitory feedback. When the empirically observed temporal buildup of the SON inhibitory response is not incorporated in the network model, ITD sensitivity decreases sharply. Further, the presence of reciprocal inhibitory connections between the two SONs increases the stability of ITD coding in the NL on both sides of the brain.

SON feedback inhibition generally maintains rate-ITD sensitivity in NL by preserving the coincidence detecting ability of NL on the inputs coming from the left and right NM. SON contributes to robust coincidence detection in NL through a dual mechanism: indirectly, by inhibiting NM, reducing the afferent rate to NL, and directly, by inhibiting NL itself.

## 4.1 Feedback inhibition

A previous model by Peña and colleagues (1996) included only *forward* connectivity from SON to a single NL cell model. We constructed a bilateral network model with feedback that includes both forward and *backward* connectivity observed in bird anatomy. Both models demonstrate that forward connections provide sound-level dependent inhibition, maintaining ITD sensitivity in NL across level. Both models also indicate that inhibition causes the greatest improvement in ITD sensitivity at the highest sound levels, where sensitivity is most reduced without inhibition. While inhibition improves ITD sensitivity across sound level in both feedback and forward models, we highlight two additional properties gained with feedback connectivity.

First, the reciprocal inhibitory connections between SONs improve ITD coding in NL. Including inhibitory coupling between the left and right SONs, in addition to each of the left- and right-side SON inhibitory loops, increases the robustness of ITD coding, both spatially (across the NL in the two hemifields), and temporally (over the entire stimulus duration). With SON inhibition to the ipsilateral targets only (or when excitatory connections are specified between the left and right SON cells), excessive inhibition can occur, significantly reducing ITD sensitivity in NL. In the actual physiological system, inhibitory connections between the two SON nuclei could serve to improve the ITD coding stability in NL by regulating the amount of inhibition delivered to the two sides. *In vitro* physiology in conjunction with neuroanatomical tracing and neurotransmitter-receptor staining studies could test whether the SON-to-SON projections are inhibitory and GABAergic, as predicted by our model.

Second, the model demonstrates that the feedback connectivity from NL to SON can impart ITD sensitivity in the SON inhibition. As a result, the SON response can be higher during in-phase versus out-of-phase stimulation (see Fig. 4, Right SON). Consequently, NM response is more inhibited, and therefore lower during in-phase versus out-of-phase stimulation to the NL (see Fig. 4, Right NM). These predictions depend on the small number of neurons and point-to-point connectivity specified in our network model. In the actual system, any potential ITD sensitivity observed in NM would hypothetically decrease as the amount of convergence increased from different best ITD tuned NL cells to a single SON cell, thus smearing-out ITD sensitivity in SON, and therefore NM. Similarly, greater convergence from SON cells with different ITD dependencies to a single NM cell would also presumably reduce any ITD sensitivity in NM. The fact that the projection from SON to NM appears to be broadly tuned as opposed to tonotopic (Burger et al. 2005) could be consistent with the possibility that multiple SON cells converge onto a single NM cell. Nevertheless, our simulations provide rationale to investigate ITD sensitivity in SON and NM *in vivo*.

#### 4.1.1 Comparison with other models with inhibition

Forward inhibition has been demonstrated in the mammalian medial superior olive (MSO) (Grothe and Sanes 1994; Smith et al. 2000; Brand et al. 2002). Since the avian inhibitory feedback circuit appears suited to maintain ITD sensitivity over variations in sound-level, the mammalian inhibitory system may also play a similar role. Assuming that the discharge rate of the mammalian inhibitory input is dependent on sound-level, greater inhibition at higher levels could hypothetically protect ITD sensitivity in the MSO (cf.

Reed and Durbeck 1995). One difference with mammalian models which have implemented phase-locked forward inhibition is that inhibition can influence a shift in the rate-ITD curve (Brand et al. 2002; Zhou et al. *in press*). Rate-ITD curves, however, do not shift with inhibitory feedback in our model of the avian system.

## 4.2 Dynamic effects of inhibition

Long-lasting inhibitory responses (i.e.,  $\geq 50$  ms) have been demonstrated *in vitro* in the chicken. The duration of the SON inhibitory response increased with greater input (Yang et al. 1999; Lu and Trussell 2000; Monsivais et al. 2000), with buildup extending to one second in NL (Yang et al. 1999). Also the EPSPs measured in single SON cells were relatively slow, on the order of 40 msec (Yang et al. 1999). We incorporated these empirically observed attributes into our network model and found that cell rates generally decrease over hundreds of milliseconds, while rate-ITD sensitivity in NL progressively increased.

### 4.2.1 Comparison with synaptic depression

The improvement in rate-ITD sensitivity demonstrated in this study is much slower than that found in a model of NL that incorporated synaptic depression observed in the chick NM to NL synapse (Cook et al. 2003). The timecourse of depression observed in the NM-to-NL synapse was on the order of tens of milliseconds (Kuba et al. 2002; Cook et al. 2003). In the functioning system, we speculate that synaptic depression may operate on a short-term timescale in conjunction with SON inhibition operating on a longer-term timescale.

### 4.2.2 Comparison with *in vivo* data

Our simulations are in general agreement with *in vivo* findings in owl that GABA sharpens the ITD sensitivity of NL (Fujita and Konishi 1991; Takahashi and Konishi 2002). The responses in our model, however, are slower than those observed in owl (Fujita and Konishi 1991; Peña et al. 1996; Viete et al. 1997; Takahashi and Konishi 2002). In the owl data, steady state responses appear to have been reached in response to 100-msec stimuli (e.g., see Peña et al. 1996, Fig. 1B-C). We propose the following five possibilities for the timecourse differences between the model and these *in vivo* data: 1) 100-ms stimuli may have been too short for a possible slow component to be seen *in vivo*, 2) species differences between the owl and chicken, 3) anesthesia may have influenced the *in vivo* responses, 4) the low temperature (i.e., room temperature) that *in vitro* experiments were conducted, on which we based our model parameters, and 5) our simulations were always started with the same set of initial values of states. Points 4 and 5 are discussed in the following paragraphs.

Our model parameters were based on *in vitro* experiments conducted at room temperature (Yang et al. 1999). Lower temperatures could increase the duration of effects observed *in vitro* compared to those occurring *in vivo* (Funabiki et al. 1998; Kuba et al. 2003). For example, Funabiki and colleagues (1998) showed that the timecourse of EPSPs in NL was significantly shorter at *in vivo*-like temperatures compared to room temperature, particularly when GABA was applied. It is possible that the temporal buildup of SON inhibition may also be reduced at body temperatures. However, temporal buildup was also demonstrated in slice at *in vivo*-like temperatures of 35°C (Lu and Trussell 2000). Moreover, Lu and Trussell (2000) in the same study demonstrated evoked inhibitory

plateau currents that lasted a few hundred milliseconds (see Lu and Trussell 2000, Fig. 1(iv)). The recovery time constants specified in our model that control the dynamics of the membrane time constant and voltage threshold in model cells rarely exceeded 500 ms. A 500 ms upper limit of inhibitory buildup seems consistent with the hundreds of millisecond long plateau currents observed empirically at 35°C.

Our simulations used the same default set of initial values at the start of each stimulus presentation (independent of input history or stimulus level). In the functioning system with continuous sound exposure and the presence of spontaneous activity, the SON feedback system may be continually “primed”, allowing the SON to provide more or perhaps less inhibition in response to high or low sound-levels. The physiological system may be in an “optimal ready-state” that is able to respond efficiently across a range of input levels. Response times *in vivo* may therefore be faster than those predicted from *in vitro* conditions.

Physiological studies could further elucidate the effects of SON GABAergic inhibition, specifically on NA, NM, and possibly on contralateral SON. Of interest would be whether the magnitudes and durations of the observed inhibitory responses are on the order of those observed *in vitro* in NL by Yang and colleagues (1999). Moreover, *in vivo* studies in chicken auditory brainstem using multibarrel recording electrodes with bicuculline would be useful to compare baseline responses (which would presumably be observed *with* physiological SON GABAergic inhibition intact), with responses obtained when bicuculline is administered (to block GABAergic effects). Results could be compared to similar experiments in owl (Fujita and Konishi 1991). Based on our simulations, response timecourses could speed up if GABAergic responses are blocked.

### 4.2.3 Temporal buildup and dynamic range

Our simulations specify a discharge rate range for SON that is compatible with that observed *in vitro* by Yang and colleagues (1999). The inclusion of the empirically observed temporal buildup of inhibitory response significantly increases the amount of rate-ITD modulation observed in NL. This finding could suggest that the temporal buildup of inhibition may be a mechanism by which a single SON cell, despite a relatively low firing rate, can provide significant inhibition/modulation on its targets. Lu and Trussell (2000) demonstrated that temporal buildup of inhibition occurred as a result of the asynchronous synaptic release of GABA as a consequence of increased SON fiber stimulation. Our model suggests that the temporal buildup of inhibition significantly increases the ITD sensitivity of NL at high levels. SON fiber synaptic specializations could therefore underlie the increase in the dynamic range of the ITD coding system.

## 4.3 Study limitations

One limitation of our study is that we specified SON inhibition to modulate a target cell's membrane time constant and threshold, without affecting its membrane voltage. On the one hand, GABAergic input from SON has been demonstrated to be depolarizing (Lu and Trussell 2001; Monsivais and Rubel 2001), even causing occasional spiking (Lu and Trussell 2001; Lu et al. *in press*). On the other hand, the GABA released from SON fibers could be limited by presynaptic GABA-B receptors, whose activation has been shown to suppress GABA-evoked discharges (Lu et al. *in press*). Further, because GABA-induced spiking was most reliable only at the onsets of (phasic) input trains (Lu and Trussell 2001),

we suspect a negligible discharge rate to steady-state inputs, like those used in the present study. Moreover, the effect of inhibition on membrane voltage may not be as critical as the absolute conductance change (i.e., the shunting effect) of the inhibitory synapse itself. A physiologically-detailed model of NL showed similar levels of ITD sensitivity regardless of whether the inhibitory input from SON was specified to be depolarizing or hyperpolarizing (Grau-Serrat et al. 2003). Future empirical and modeling studies could further explore the impact of SON-induced depolarization, particularly under phasic stimulation conditions.

A second limitation of our study is that the leaky-integrate-and-fire (LIF) type cell models used do not contain ion channels (such as low threshold potassium channels) or dendrites, both of which can reduce response to less-coincident (e.g., out-of-phase) inputs (cf. Reyes et al. 1996; Agmon-Snir et al. 1998; Cook et al. 2003; Svirskis et al. 2003; Grau-Serrat et al. 2003; Dasika 2004; Svirskis et al. 2004). Ion channels and dendrites may help maintain ITD sensitivity in NL by keeping in-phase responses consistently greater than out-of-phase responses. LIF models, on the other hand, can exhibit “reverse-modulation” under certain high-level stimulation conditions, such that the out-of-phase response can actually *exceed* the in-phase response (cf. Reed and Durbeck 1995; Peña et al. 1996). The fact that LIF models can demonstrate reverse-modulation may actually provide a more stringent test of SON feedback inhibition. The out-of-phase response needs to be reduced significantly, while the in-phase response should not be excessively reduced, in order to achieve rate-ITD modulation, under stimulus conditions that induce reverse-modulation. We found that the inclusion of SON inhibitory feedback in the network model could change responses in NL from significant reverse-modulation to modulation [data not shown; percentage-of-modulation without SON feedback was  $-67\%$ ;

percentage-of-modulation with SON feedback was +18%;  $f = 450$  Hz;  $R = 450$  spikes/sec to the two sides; stimulus length = 2 sec (steady-state responses occurred by about 1 sec)]. SON inhibition therefore appears to be both potent and adaptable, providing an appropriate amount of feedback to achieve ITD sensitivity in NL.

#### 4.4 Concluding Remarks

The avian brainstem network embodying SON inhibitory feedback demonstrates robust ITD coding across sound-level. The effects of feedback inhibition are similar to those derived from forward inhibition, with added stability.

Future studies could test the effects of SON inhibitory feedback combined with the inclusion of synaptic depression (cf. Cook et al. 2003). Specific contributions of each mechanism, as well as net effects due to both mechanisms, should be determined. We speculate that the ITD coding system would be most robust when both SON network inhibition *and* synaptic depression are jointly incorporated. Both mechanisms are presumably acting in parallel in the functioning organism, albeit possibly at different timescales — with depression adjusting the synaptic strength within milliseconds, and SON inhibition providing long-term modulation over hundreds of milliseconds. Such studies would further increase our understanding of how neural specializations expand the dynamic range of the auditory system.

## 5 Text Footnotes

<sup>1</sup>The physical headsize of the chicken is relatively small, producing negligible acoustic interaural level differences in response to low frequency stimulation. However, interaural middle-ear coupling has been demonstrated to cause significant differences between the levels of the cochlear microphonic signals in each ear (on the order of two-times) in response to low-frequency, free-field, off-center tonal stimuli (Hyson et al. 1994).

<sup>2</sup>An analytical solution was convenient because  $V_m$  needed to be calculated only at the time of inputs.

<sup>3</sup>A similar measure was used by Grau-Serrat et al. (2003) to report the degree of rate-ITD modulation in model NL.

<sup>4</sup>In this discussion, we assume that the relative extent of rate-ITD modulation in NL reflects the sensitivity of NL to changes in ITD.

## 6 Acknowledgments

We thank Drs. Michael Burger and Edwin Rubel for their valuable comments on this manuscript and for sharing insight and data on the avian auditory brainstem. We also thank Dr. Wil Howitt for helpful advice on the computational implementation of the simulations. We thank the two anonymous reviewers and Dr. Catherine Carr whose comments greatly improved this paper.

### Grants

This work was supported by NIH: NIDCD DC00100 (VKD, HSC); NINDS NS24425 (JAW); and NIDCD DC01641 (LHC).

## 7 References

- Agmon-Snir H, Carr CE, and Rinzel J.** The role of dendrites in auditory coincidence detection. *Nature* 393(6682): 268–272, 1998.
- Blauert J.** *Spatial hearing: The Psychophysics of Human Sound Localization (Revised edition)*. Cambridge, MA: The MIT Press, 1997.
- Brand A, Behrend O, Marquardt T, McAlpine D, and Grothe B.** Precise inhibition is essential for microsecond interaural time difference coding. *Nature* 30(417): 543–547, 2002.
- Burger RM, Cramer KS, Pfeiffer JD, and Rubel EW.** Avian superior olivary nucleus provides divergent inhibitory input to parallel auditory pathways. *J Comp Neurol* 481(1): 6-18, 2005.
- Carr CE and Konishi M.** A circuit for detection of interaural time differences in the brain stem of the barn owl. *J Neurosci* 10(10): 3227–3246, 1990.
- Colburn HS, Zhou Y, and Dasika VK.** Inhibition in models of coincidence detection. In: *Auditory signal processing: physiology, psychoacoustics, and models*, edited by Pressnitzer D, de Cheveigne A, McAdams S, and Collet L. New York: Springer, 2004, p. 299–305.
- Cook DL, Schwindt PC, Grande LA, and Spain WJ.** Synaptic depression in the localization of sound. *Nature* 421(6918): 66–70, 2003. (Corrigenda. *Nature* 423: 197 May 2003)
- Dasika VK.** Dendritic models and the influence of spatial coupling on time-delay sensitivity. In: *Models of auditory brainstem coincidence-detector neurons*. PhD

Dissertation, Boston University, 2004, p. 67–101.

**Dayan P and Abbott LF.** Mathematical Appendix. In: *Theoretical Neuroscience: Computational and Mathematical Modeling of Neural Systems*, edited by Sejnowski TJ and Poggio T. Cambridge, MA: The MIT Press, 2001, p. 404–405.

**Fujita I and Konishi M.** The role of gabaergic inhibition in processing of interaural time difference in the owl's auditory system. *J Neurosci* 11(3): 722–739, 1991.

**Funabiki K, Koyano K, and Ohmori H.** The role of gabaergic inputs for coincidence detection in the neurones of nucleus laminaris of the chick. *J Physiol* 508 (Pt 3): 851–869, 1998.

**Goldberg JM and Brown PB.** Response of binaural neurons of dog superior olivary complex to dichotic tonal stimuli: some physiological mechanisms of sound localization. *J Neurophysiol* 32: 613–636, 1969.

**Grau-Serrat V, Carr CE, and Simon JZ.** Modeling coincidence detection in nucleus laminaris. *Biol Cybern* 89(5): 388–396, 2003.

**Grothe B.** New roles for synaptic inhibition in sound localization. *Nat Rev Neurosci* 4(7): 540–50, 2003.

**Grothe B and Sanes DH.** Synaptic inhibition influences the temporal coding properties of medial superior olivary neurons: an in vitro study. *J Neurosci* 14(3 Pt 2): 1701–1709, 1994.

**Hyson RL, Overholt EM, and Lippe WR.** Cochlear microphonic measurements of interaural time differences in the chick. *Hear Res* 81(1–2): 109–118, 1994.

**Hyson RL, Reyes AD, and Rubel EW.** A depolarizing inhibitory response to gaba in brainstem auditory neurons of the chick. *Brain Res* 677(1): 117–126, 1995.

**Jeffress LA.** A place theory of sound localization. *J Comp Physiol Psychol* 41: 35–39, 1948.

**Joris PX, Carney LH, Smith PH, and Yin TC.** Enhancement of neural synchronization in the anteroventral cochlear nucleus. I: Responses to tones at the characteristic frequency. *J Neurophysiol* 71(3): 1022–1036, 1994.

**Kuba H, Koyano K, and Ohmori H.** Synaptic depression improves coincidence detection in the nucleus laminaris in brainstem slices of the chick embryo. *Eur J Neurosci* 15(6): 984–990, 2002.

**Kuba H, Yamada R, Ohmori H.** Evaluation of the limiting acuity of coincidence detection in nucleus laminaris of the chicken. *J Physiol* 552(Pt 2): 611–620, 2003.

**Lachica EA, Rübsamen R, and Rubel EW.** Gabaergic terminals in nucleus magnocellularis and laminaris originate from the superior olivary nucleus. *J Comp Neurol* 348(3): 403–418, 1994.

**Lu T and Trussell LO.** Inhibitory transmission mediated by asynchronous transmitter release. *Neuron* 26(3): 683–694, 2000.

**Lu T and Trussell LO.** Mixed excitatory and inhibitory gaba-mediated transmission in chick cochlear nucleus. *J Physiol* 535(Pt 1): 125–131, 2001.

**Lu Y, Burger RM, and Rubel EW.** Gaba-b receptor activation modulates gaba-a receptor-mediated inhibition in chicken nucleus magnocellularis neurons. *J Neurophysiol* October 13, 2004; 10.1152/jn.00786.2004.

**Monsivais P and Rubel EW.** Accommodation enhances depolarizing inhibition in central neurons. *J Neurosci* 21(19): 7823–7830, 2001.

**Monsivais P, Yang L, and Rubel EW.** Gabaergic inhibition in nucleus magnocellularis: implications for phase locking in the avian auditory brainstem. *J Neurosci* 20(8): 2954–2963, 2000.

**Overholt EM, Rubel EW, and Hyson RL.** A circuit for coding interaural time differences in the chick brainstem. *J Neurosci* 12(5): 1698–1708, 1992.

**Peña JL, Viete S, Albeck Y, and Konishi M.** Tolerance to sound intensity of binaural coincidence detection in the nucleus laminaris of the owl. *J Neurosci* 16(21): 7046–7054, 1996.

**Raman IM, Zhang S, and Trussell LO.** Pathway-specific variants of ampa receptors and their contribution to neuronal signaling. *J Neurosci* 14(8): 4998–5010, 1994.

**Reed MC and Durbeck L.** Delay lines and auditory processing. *Comments on modern biology, Volume C: Comments on theoretical biology* 3(6): 441–461, 1995.

**Reyes AD, Rubel EW, and Spain WJ.** Membrane properties underlying the firing of neurons in the avian cochlear nucleus. *J Neurosci* 14(9): 5352–5364, 1994.

**Reyes AD, Rubel EW, and Spain WJ.** In vitro analysis of optimal stimuli for phase-locking and time-delayed modulation of firing in avian nucleus laminaris neurons. *J Neurosci* 16(3): 993–1007, 1996.

**Smith AJ, Owens S, Forsythe ID.** Characterisation of inhibitory and excitatory postsynaptic currents of the rat medial superior olive. *J Physiol* 529(3): 681–698, 2000.

**Soares D, Chitwood RA, Hyson RL, and Carr CE.** Intrinsic neuronal properties of the chick nucleus angularis. *J Neurophysiol* 88(1): 152–162, 2002.

**Sullivan WE and Konishi M.** Segregation of stimulus phase and intensity coding in the cochlear nucleus of the barn owl. *J Neurosci* 4(7): 1787–1799, 1984.

**Svirskis G, Dodla R, Rinzel J.** Subthreshold outward currents enhance temporal integration in auditory neurons. *Biol Cybern* 89(5): 333–340, 2003.

**Svirskis G, Kotak V, Sanes DH, Rinzel J.** Sodium along with low-threshold potassium currents enhance coincidence detection of subthreshold noisy signals in MSO neurons. *J Neurophysiol* 91(6): 2465–2473, 2004.

**Takahashi Y and Konishi M.** Manipulation of inhibition in the owl's nucleus laminaris and its effects on optic tectum neurons. *Neuroscience* 111(2): 373–378, 2002.

**Tuckwell H.** The Lapicque of the nerve cell. In: *Introduction to the theoretical neurobiology, Volume 1*. Cambridge: Cambridge University Press, 1988, p. 85–123.

**Viete S, Peña JL, and Konishi M.** Effects of interaural intensity difference on the processing of interaural time difference in the owl's nucleus laminaris. *J Neurosci* 17(5): 1815–1824, 1997.

**Warchol ME and Dallos P.** Neural coding in the chick cochlear nucleus. *J Comp Physiol [A]* 166(5): 721–734, 1990.

**Yang L, Monsivais P, and Rubel EW.** The superior olivary nucleus and its influence on nucleus laminaris: a source of inhibitory feedback for coincidence detection in the avian auditory brainstem. *J Neurosci* 19(6): 2313–2325, 1999.

**Zhou Y and Colburn HS.** A neural model of an MSO neuron. *Abstracts of the Midwinter Research Meeting/Association for Research in Otolaryngology* 1514, 2003.

Available at: [http://www.aro.org/archives/2003/2003\\_1514.html](http://www.aro.org/archives/2003/2003_1514.html)

**Zhou Y, Carney LH, and Colburn HS.** A model for ITD sensitivity in the MSO: Interaction of excitatory and inhibitory synaptic inputs, channel dynamics, and cellular morphology. *J Neurosci*, *accepted*.

## 8 Figure legends

**Figure 1.** Network model block diagram. Excitatory connections are shown as solid black lines. Inhibitory connections are shown as dashed lines. One SON, NL, and NA cell is represented from each of the two sides. Ten NM cells are represented per side. Three phase-locked auditory-nerve fibers, “AN PL fibers”, innervate each NM cell. Each numbered AN PL fiber on a given side represents one independent phase-locked auditory-nerve fiber — all fibers on both sides share the same frequency and vector strength. An independent non-phase-locked auditory-nerve fiber, “AN nonPL fiber”, excites each NA cell.

**Figure 2.** Illustration of the effects of inhibition on an adapting LIF cell model. Four different inhibitory conditions are represented across the four columns in rows **A-D**. Row **A** shows  $\tau_{\tau_m}$  and/or  $\tau_{V_T}$ ; row **B** shows  $\tau_m$ ; row **C** shows  $V_m$  (as the shaded region between the minimum and the maximum voltage values occurring within each stimulus period) and  $V_T$ ; and row **D** shows the moving-averaged response rates. The same excitatory and inhibitory input time sets were used for each of the four inhibitory conditions. Panels **E** and **F** show the details of the voltage responses represented in the third and fourth panels of row **C**. Input rasters superimposing the 20 independent excitatory inputs are shown below the voltage traces in **E** and **F** (inhibitory input rasters are not shown). Cell discharges are indicated by x’s and shown above the voltage traces. In the first 10 msec (**E**), both voltage traces were identical because no inhibitory inputs occurred (the response reflects that of a standard LIF model). In the last 10 msec (**F**), however, the membrane time constant had decreased (as seen in row **B**, fourth versus third panels), decreasing  $V_m$

(**F**, thick black line) in comparison to when the membrane time constant was unaffected (**F**, thick gray line). Excitatory inputs that occurred within 1 ms of a cell discharge were ignored as a consequence of the specified absolute refractory period. The pairs of dotted lines shown in **E** and in the insets of the second panels of **A** and **B** depict the initial slope of decay at two different state variable magnitudes. For this figure: Twenty phase-locked inputs excited an adapting LIF cell, each with an average rate of 300 spikes/sec. The average rate of the single inhibitory input fiber was 75 spikes/sec. No time delays or synaptic delays were added to any of the inputs. An excitatory input caused a depolarization ( $V_m^{inc}$ ) of 0.2 to the membrane voltage, the initial threshold voltage  $V_T^0$  was 1,  $V_T^{inc}$  was .05, and  $V_T^{ceil}$  was 2. The refractory period was 1 ms.

**Figure 3.** Inhibition does not affect ITD modulation at low input rates. Auditory nerve input rate is 150 spikes/sec to both the left and right sides. Response rate is shown for each of the modeled NL, NA, and SON cells from the left and right sides. Each NM plot shows the average response rate across the ten NM cells on the corresponding side. **Solid lines** indicate cell responses without inhibitory feedback, whereas **dashed lines** indicate cell responses to the identical stimuli set, when inhibitory feedback is included. Stimuli were delivered with one of two ITDs, either: 1) so that input from the left and right NM arrived *in-phase* at the *right* NL (indicated by the points **without triangles**), or 2) so that the inputs from the left and right NM cells arrived *out-of-phase* at the *right* NL (indicated by the points **with triangles**). Response asymmetries occur across the two sides because the left and right NL are tuned to different best ITDs (see Methods).

**Figure 4.** Inhibition improves ITD modulation at high input rates. Input rates are 450 spikes/sec to both the left and right sides. The format is the same as Fig. 3.

**Figure 5.** Rate-ITD curves in the right NL for different epochs of time during the response. Input rate is 450 spikes/sec to the two sides. The ITD axis has been centered with respect to the in-phase delay at the right NL. The parameter (which has units in ms) corresponds to the center of the 100 ms moving average window. For each window location, the response to each ITD over one period was computed. Values at negative ITDs are just the positive values reflected around the ITD=0 point and re-plotted. At the stimulus onset, the combination of the synaptic delay and the ITD caused a total delay of 1.6 ms to the right NL; this delay caused one response period to be omitted from the response, which explains the slight decrease (10 spikes/sec) in the response during the first window. (This slight decrease in rate at the onset can also be seen in Fig. 6).

**Figure 6.** Responses in the right NL for various input rate conditions, for both balanced (left column) and imbalanced (right column) input rates from the two sides. The additional pair of dotted lines in **E** show the responses when the SON temporal buildup mechanism is limited by setting  $\tau_{\tau_m}^{ceil}$  and  $\tau_{V_T}^{ceil}$  equal to 50ms (as opposed to 1 sec) for all cells (the in-phase response is essentially equal to the in-phase no-feedback response so it cannot be seen). Similar responses between the no-feedback and the no-temporal-buildup with feedback cases also occurred for imbalanced inputs of 150, 450 spikes/sec [data not shown].

**Figure 7.** Percentage-of-modulation for the same input conditions shown in Fig. 6. The additional dotted trace shown in **E** is the no-temporal-buildup with feedback case that

corresponds to the same condition in Fig. 6E. A similar minimal improvement in modulation for the no-temporal-buildup with feedback condition compared to the no-feedback condition occurred for imbalanced inputs of 150, 450 spikes/sec [data not shown].

**Figure 8.** Response Rates and Percentage-of-modulation in the left and right NL under three different configurations of SON feedback inhibition. Input rates are 150 spikes/sec to the left side and 450 spikes/sec to the right side. The parameter is the specific SON inhibitory feedback connectivity for three conditions: no inhibition, ipsilateral only inhibition (i.e., no inhibitory connections between the two SON in Fig. 1), and full feedback inhibition as shown in Fig. 1.

### A. Input Parameters

stimulus duration	.5sec [or 2sec]
periodic stimulation frequency ( $f$ )	600Hz [or 450Hz]
AN periodic input vector strength ( $VS$ )	.76 [or .8]
AN input rate	150, 300, or 450 spikes/sec

### B. Summary of State Variables

$V_m$	membrane voltage
$\tau_m$	membrane time constant
$\tau_{\tau_m}$	time constant that controls the dynamics of the membrane time constant
$V_T$	threshold voltage
$\tau_{V_T}$	time constant that controls the dynamics of the threshold voltage

### C. Excitatory Connections

From	To	Syn Delay	$V_m^{inc}$
AN (phase-locked)	NM	0	1
AN (non-phase-locked)	NA	0	1
NA	SON	3ms	1
NM	NL	1.5 or 1.6ms	1
NL	SON	2ms	1
SON	SON	5ms	0 [or 1]

### D. Inhibitory Connections

From	To	Syn Delay	$\tau_{\tau_m}^{inc}$	$\tau_m^{dec}$	$\tau_{V_T}^{inc}$	$V_T^{inc}$
SON	NA	5ms	0	0	50ms	.058
SON	NM	3ms	50ms	.05ms	50ms	.068
SON	NL	5ms	50ms	.04ms	0	0
SON	SON	5ms	50ms	2ms	50ms	.125

### E. Cell Parameters

Cell	Abs Refract	$\tau_{\tau_m}^{ceil}$	$\tau_m^0$	$\tau_m^{floor}$	$\tau_{V_T}^{ceil}$	$V_T^0$	$V_T^{ceil}$
NA	2ms	-	2ms	-	1sec [or 50ms]	1.168	2
NM	1.5ms	1sec [or 50ms]	.417ms	.2ms	1sec [or 50ms]	1.068	2
NL	1ms	1sec [or 50ms]	.8ms	.3ms	-	3.368	-
SON	6ms	1sec [or 50ms]	40ms	20ms	1sec [or 50ms]	2.5	5

Table 1: Table of model parameters. In **B-E**,  $V_m$ ,  $V_m^{inc}$ ,  $V_T^{inc}$ ,  $V_T^0$ , and  $V_T^{ceil}$  are all specified in the same relative units. In **C** and **D**, “Syn Delay” means synaptic/propagation delay. In **E**, “Abs Refract” represents the absolute refractory period. Dashes represent values that are not necessary since inhibitory input is not specified to affect those states. Entries enclosed in brackets ([ ]) include those tested in a limited number of situations where noted in the paper.

Figure 1:

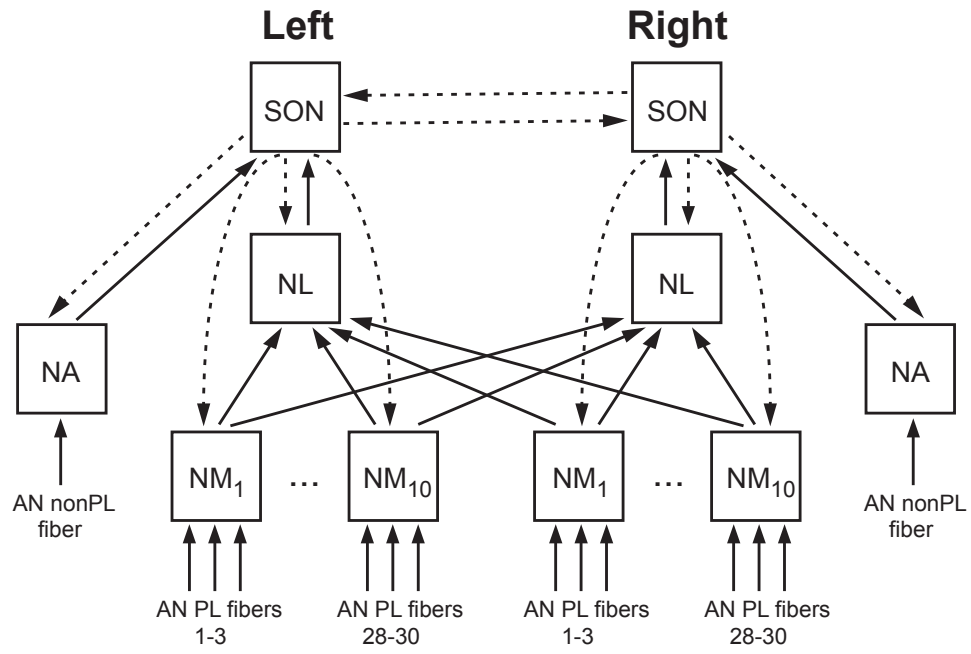
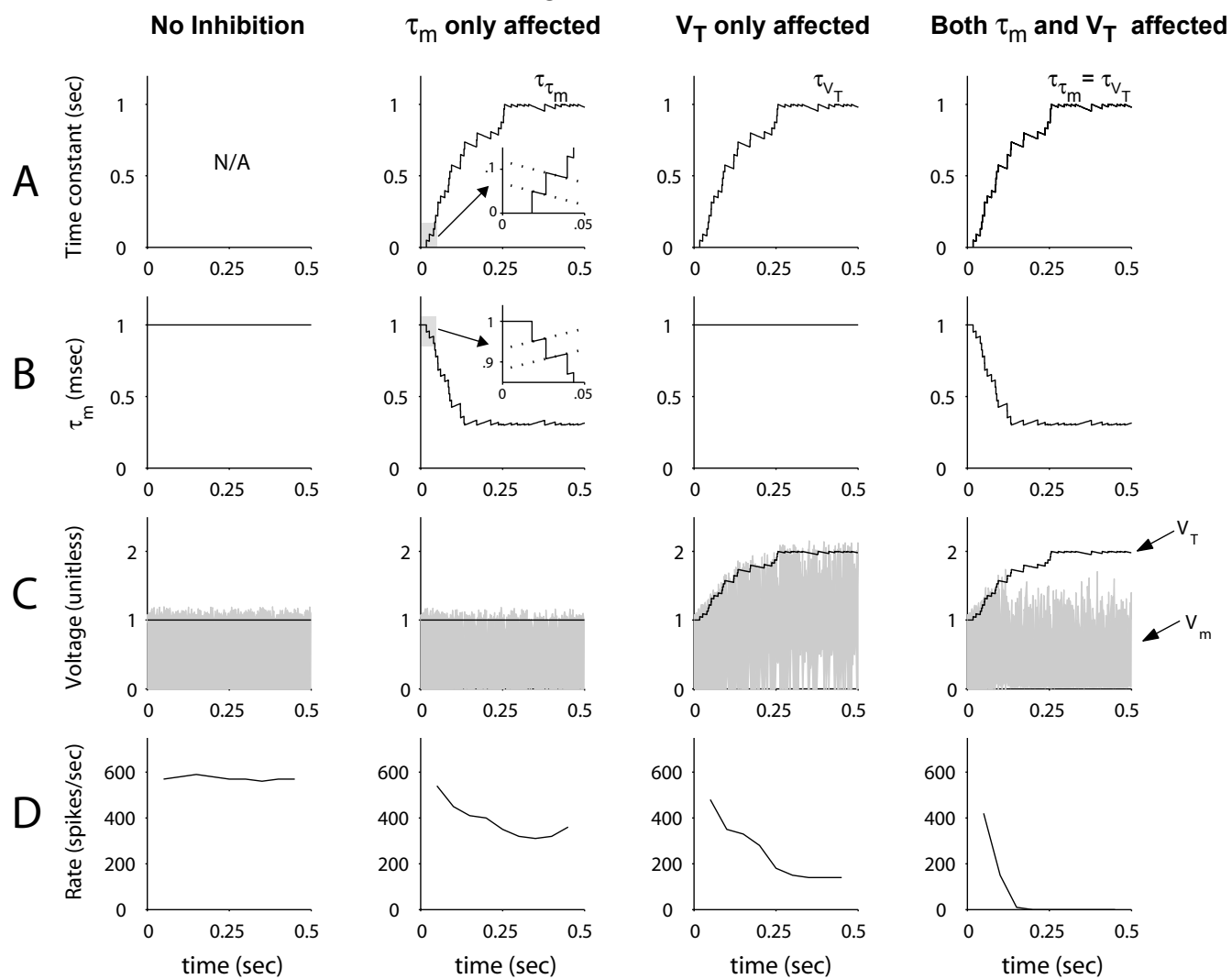


Figure 2:



Voltage responses represented in third and fourth panels of C

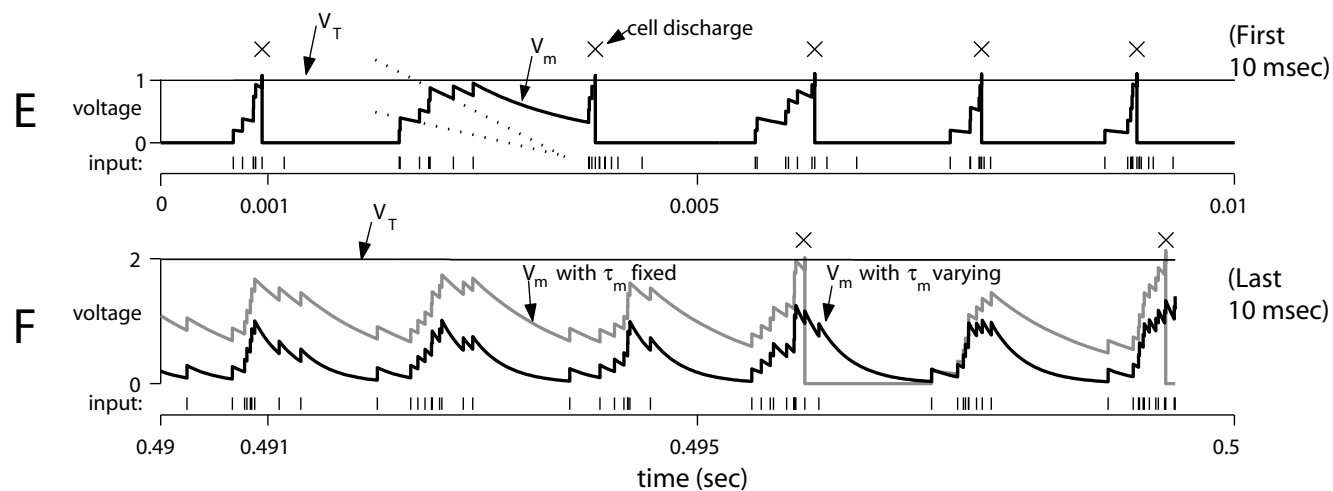


Figure 3:

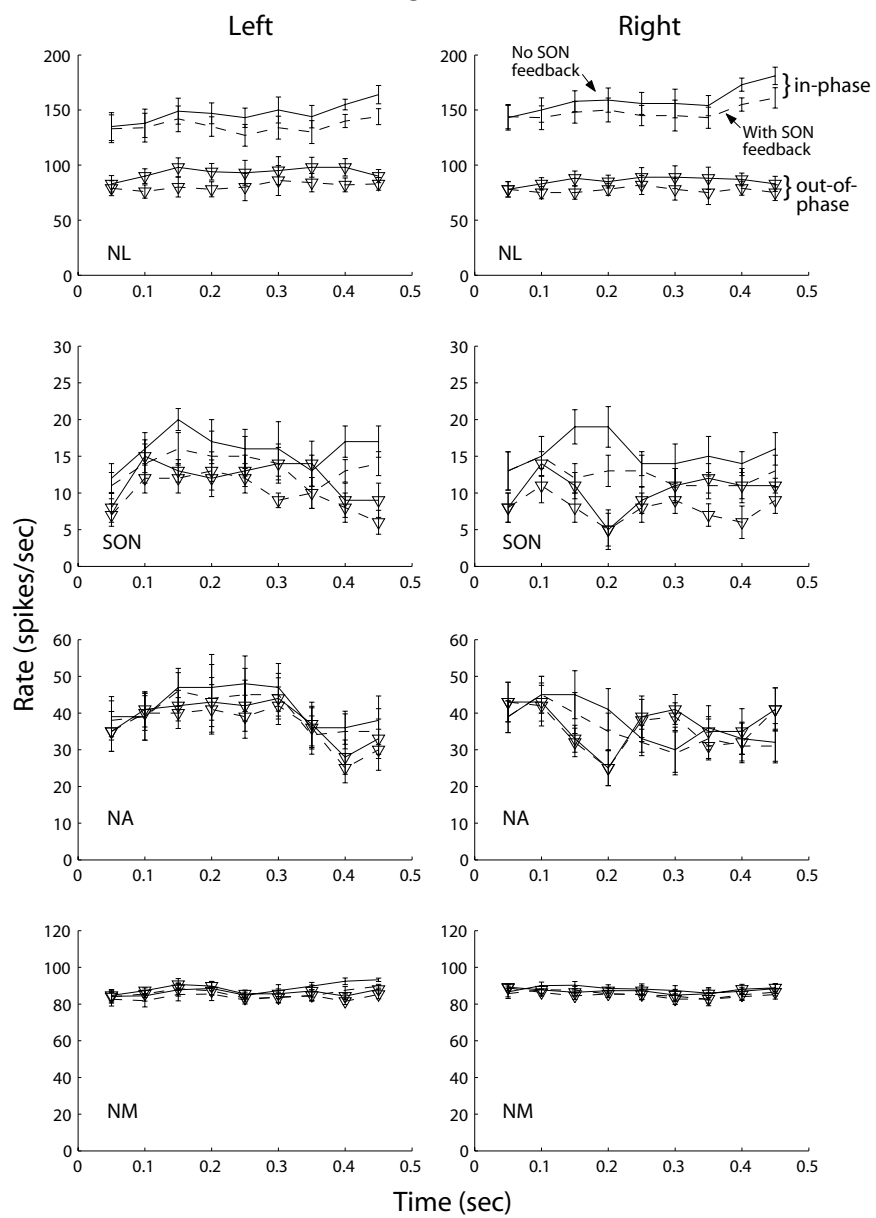


Figure 4:

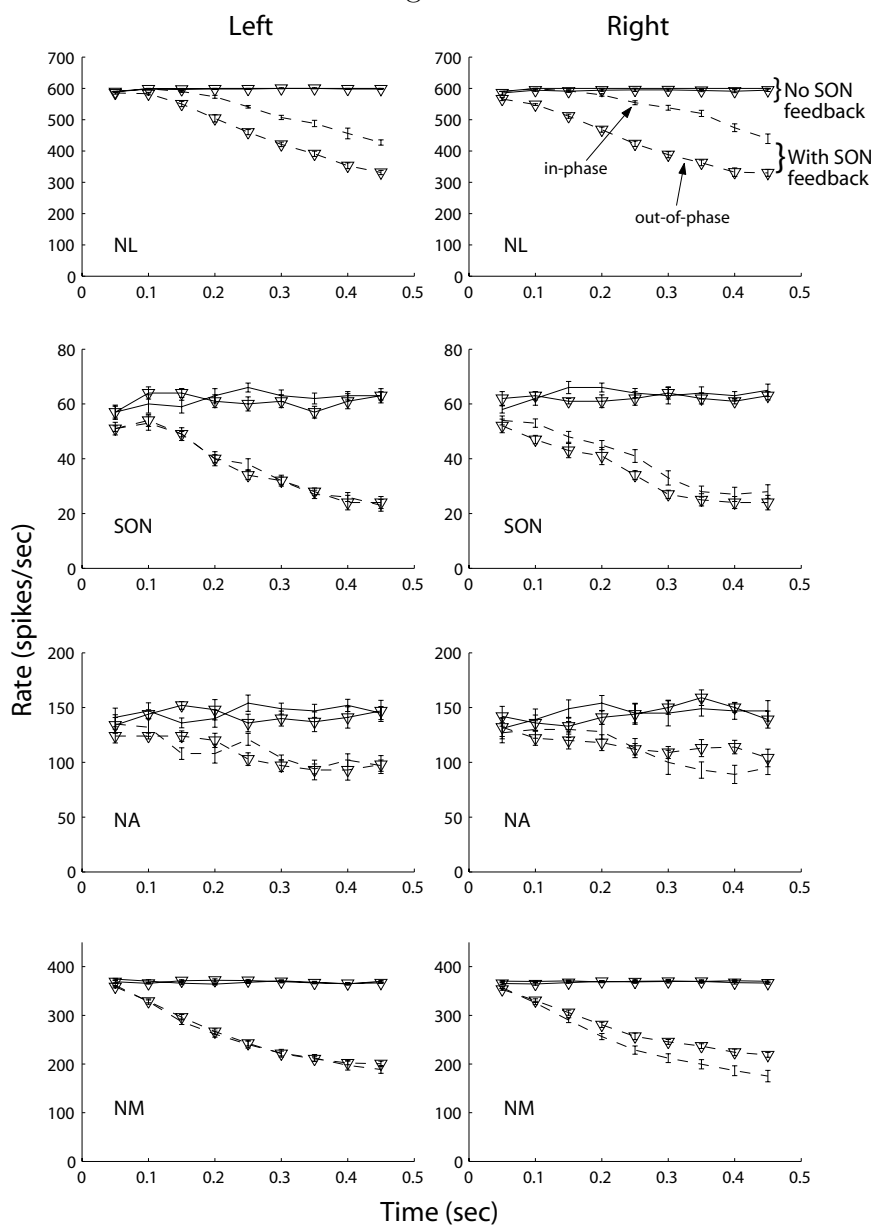


Figure 5:

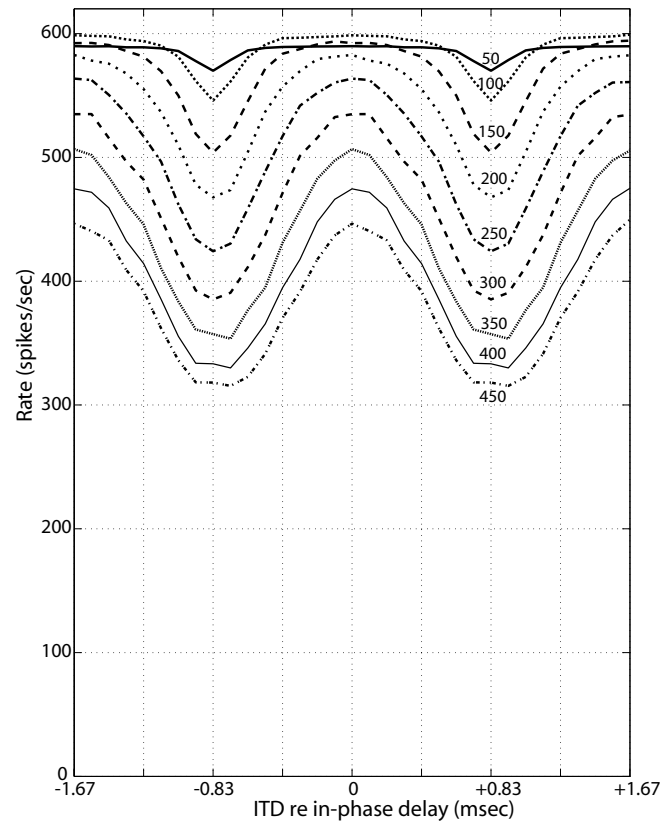


Figure 6:

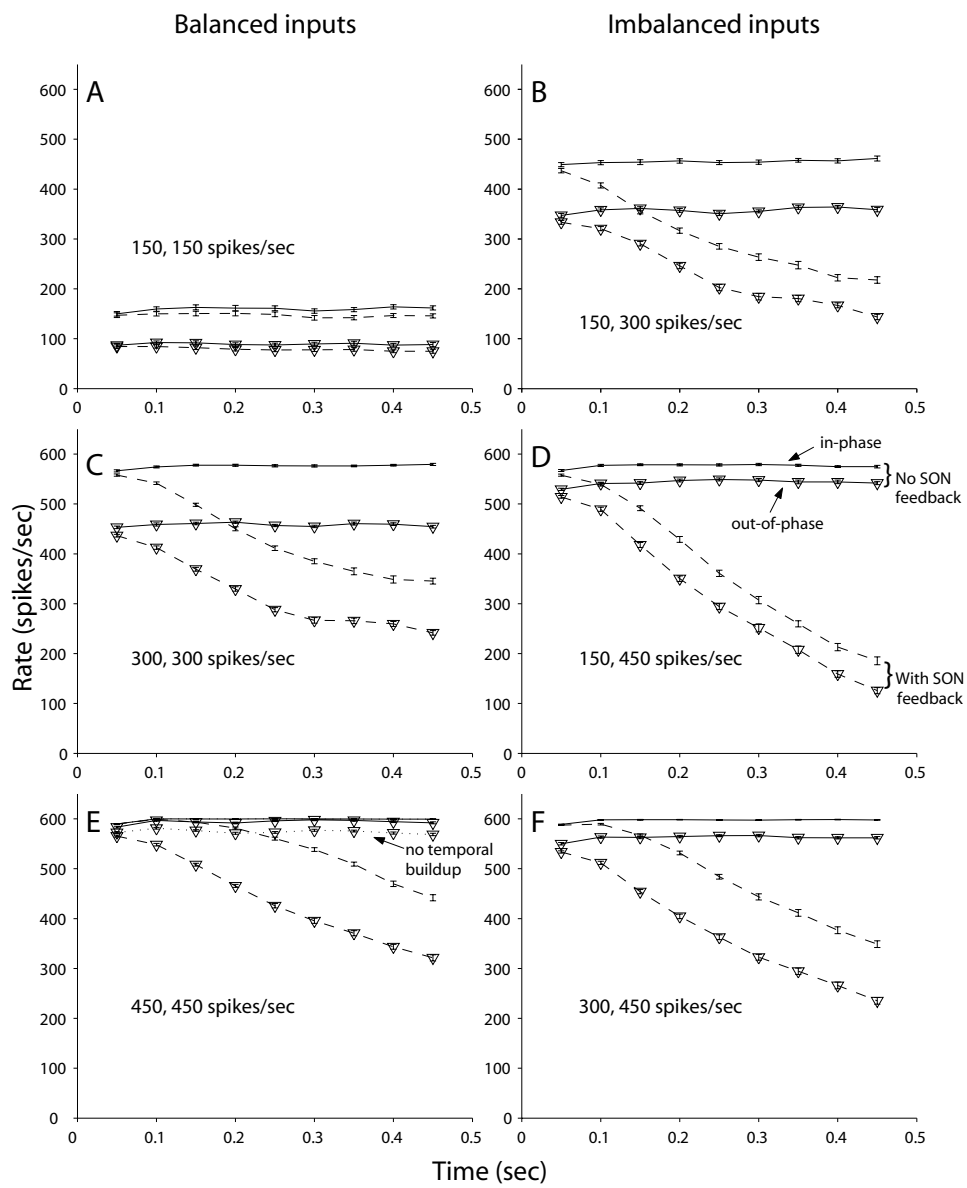


Figure 7:

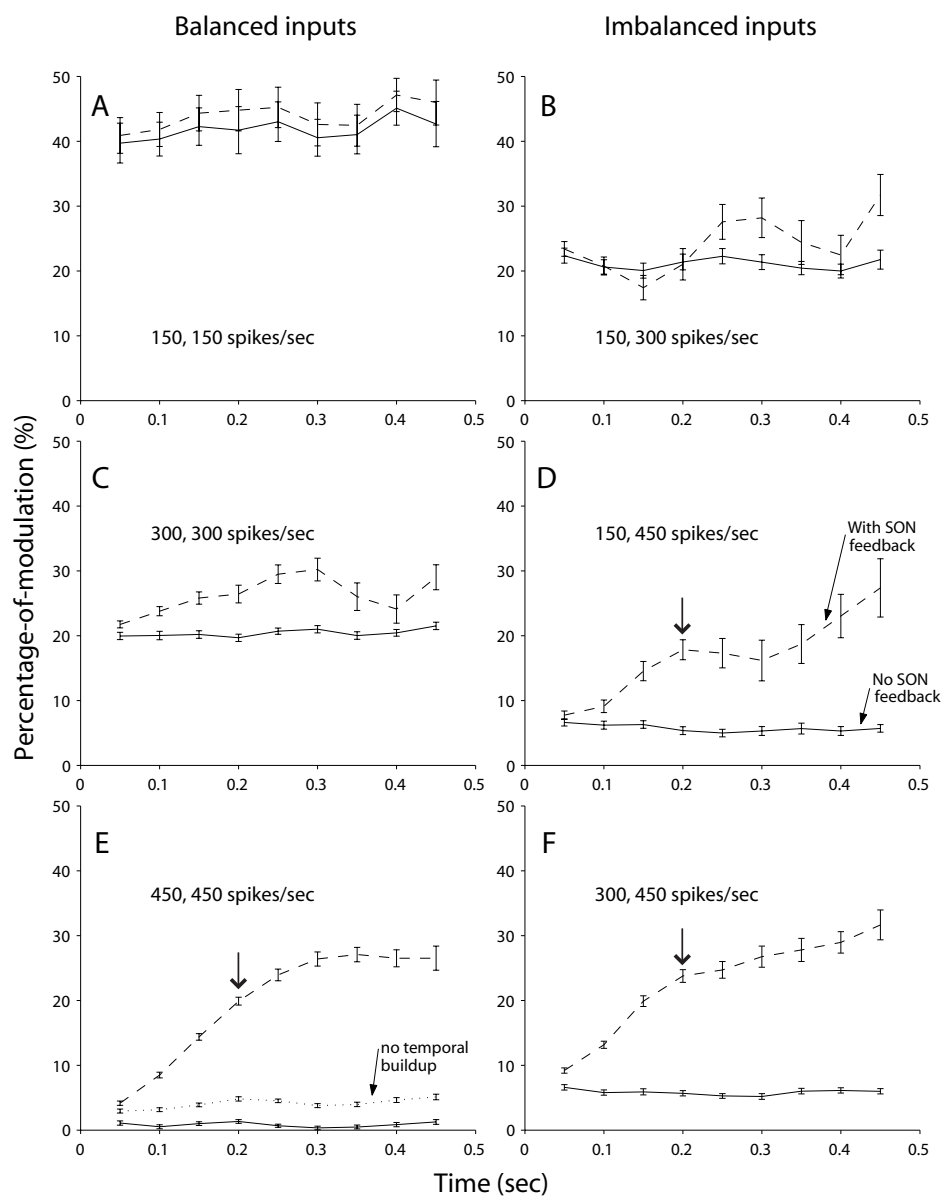
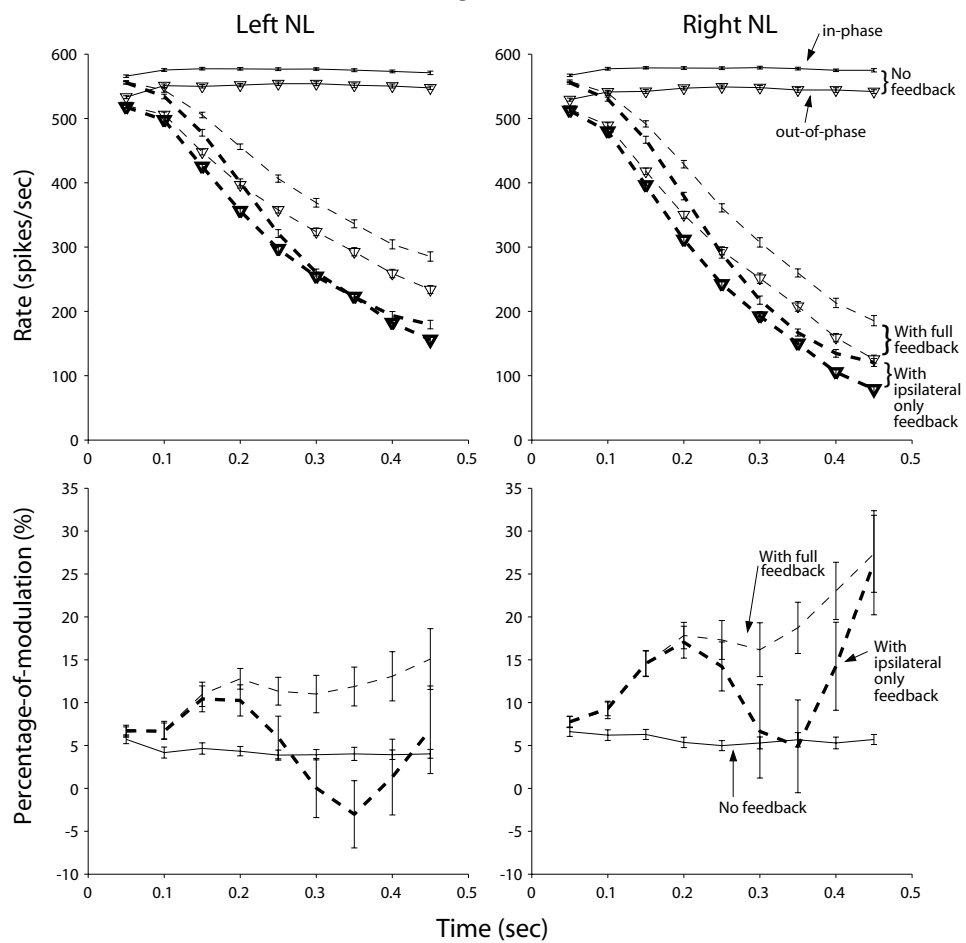


Figure 8:



## 9 Appendix

Here we provide the derivation of the expression for the membrane voltage in the adapting LIF model shown in Eq. 3. In order to derive the expression for the membrane voltage since the time of the last input event ( $t_k$ ), and before the time of the next input event, we start with Eq. 2:

$$\frac{dV_m(t)}{dt} = \frac{-V_m(t)}{\underbrace{(\tau_m(t_k^+) - \tau_m^0) \exp\left(\frac{-(t-t_k)}{\tau_{\tau_m}(t_{inh,rec}^+)}\right) + \tau_m^0}_{\tau_m(t)}}. \quad (4)$$

Equation 4 is rearranged and integrated from  $t_k^+$  to  $t$  as shown in Eq. 5:

$$\int_{t_k^+}^t \frac{dV_m(t')}{V_m(t')} = \frac{-\tau_{\tau_m}(t_{inh,rec}^+)}{\tau_m^0} \int_{t_k^+}^t \frac{\frac{1}{\tau_{\tau_m}(t_{inh,rec}^+)} \exp\left(\frac{t'-t_k}{\tau_{\tau_m}(t_{inh,rec}^+)}\right) dt'}{\exp\left(\frac{t'-t_k}{\tau_{\tau_m}(t_{inh,rec}^+)}\right) + \frac{(\tau_m(t_k^+) - \tau_m^0)}{\tau_m^0}}, \quad (5)$$

resulting in:

$$\ln \frac{V_m(t)}{V_m(t_k^+)} = \ln \left[ \left( \frac{\exp\left(\frac{t-t_k}{\tau_{\tau_m}(t_{inh,rec}^+)}\right) + \frac{(\tau_m(t_k^+) - \tau_m^0)}{\tau_m^0}}{\frac{\tau_m(t_k^+)}{\tau_m^0}} \right)^{\frac{-\tau_{\tau_m}(t_{inh,rec}^+)}{\tau_m^0}} \right]. \quad (6)$$

Equation 6 can be rewritten as:

$$\frac{V_m(t)}{V_m(t_k^+)} = \left[ \frac{\frac{\tau_m(t_k^+)}{\tau_m^0} \exp\left(\frac{-(t-t_k)}{\tau_{\tau_m}(t_{inh,rec}^+)}\right)}{1 + \frac{(\tau_m(t_k^+) - \tau_m^0)}{\tau_m^0} \exp\left(\frac{-(t-t_k)}{\tau_{\tau_m}(t_{inh,rec}^+)}\right)} \right]^{\frac{\tau_{\tau_m}(t_{inh,rec}^+)}{\tau_m^0}}, \quad (7)$$

which can be rewritten as Eq. 3.